

<https://doi.org/10.1038/s41612-024-00603-7>

Anthropogenic warming degrades spring air quality in Northeast Asia by enhancing atmospheric stability and transboundary transport

Young-Hee Ryu¹ & Seung-Ki Min^{2,3}✉

Air pollutants can travel long distances from their sources, often causing severe particulate matter (PM) pollution in downwind regions. This transboundary pollution is largely influenced by meteorology and hence its changes associated with climate change. However, the effects of anthropogenic warming on transboundary pollution remain unclear. We show that springtime PM pollution can worsen with anthropogenic warming not only in the upwind region (northern China) but also in the downwind regions (South Korea and southern Japan). The worse air quality in northern China is attributed to a shallower boundary layer due to warmer air advection in the upper levels from high-latitude Eurasia and thus increased atmospheric stability. In the downwind regions, enhanced westerly/southwesterly anomalies induced by anthropogenic warming strengthen transboundary transport. The increase in primary aerosol concentrations due to the shallower boundary layer and/or enhanced transboundary transport is ~14% in northern China, ~13% in South Korea, and ~17% in southern Japan. The elevated relative humidity due to enhanced moisture transport by the wind anomalies promotes secondary aerosol formation, which further degrades the air quality in the downwind regions. The enhancement ratio of secondary aerosols relative to changes in primary aerosols is ~1 in northern China, ~1.12 in South Korea, and ~1.18 in southern Japan due to anthropogenic warming.

Particulate matter (PM) pollution poses a serious threat to public health, particularly to 1.6 billion people in Northeast Asia^{1–3}. It is also associated with degraded visibility^{4,5}, reduced solar radiation^{6,7}, and enhanced acid deposition in ocean and soil^{8,9}. The primary cause of PM pollution has been the tremendous increase in anthropogenic emissions since the mid-20th century¹⁰. To mitigate PM pollution, countries in Northeast Asia, namely China, South Korea, and Japan, have made significant efforts to reduce anthropogenic pollutant emissions in recent decades¹¹. As a result, the annual mean PM concentrations have shown noticeable decreasing trends, particularly in the last decade (Fig. 1). For example, annual mean PM_{2.5} (PM with an aerodynamic diameter less than 2.5 μm) concentrations in northern China (Beijing-Tianjin-Hebei region, BTH region hereafter) reveal substantial decreases from

105.3 μg m⁻³ in 2013 to 36.6 μg m⁻³ in 2022 as a result of the China's clean air action plan since 2013 (Fig. 1a).

Unlike annual mean PM concentrations, however, springtime PM concentrations under high relative humidity (RH) conditions show less clear trends especially in the Seoul metropolitan area, South Korea (Fig. 1b) and southern Japan (Fig. 1c), which draws our attention. The mean PM_{2.5} or PM₁₀ (PM with an aerodynamic diameter less than 10 μm) concentrations under high RH conditions are generally much higher than their annual means, reaching almost double of the annual means. More importantly, the mean PM concentrations under high RH conditions relative to their annual mean values show increasing trends over the three regions. This implies that even though annual mean PM concentrations have decreased due to reduced emissions in recent years, PM can reach high levels under favorable

¹Department of Atmospheric Sciences, Yonsei University, Seoul, South Korea. ²Division of Environmental Science and Engineering, Pohang University of Science and Technology (POSTECH), Pohang, South Korea. ³Institute for Convergence Research and Education in Advanced Technology, Yonsei University, Incheon, Republic of Korea. ✉e-mail: skmin@postech.ac.kr

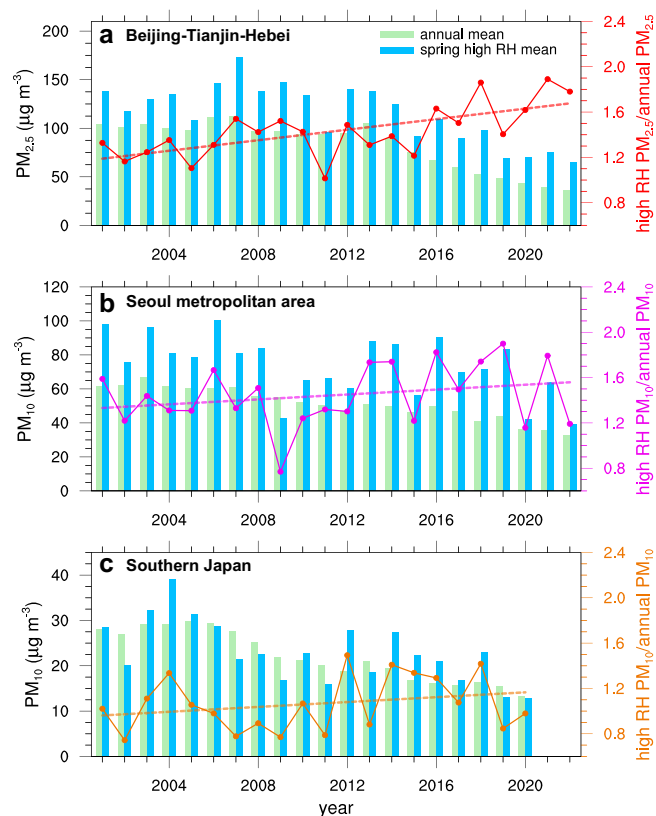


Fig. 1 | Annual mean PM concentrations, high-RH-condition PM concentrations in spring, and their ratio. Time series of annual mean PM concentration (light green bars) and springtime mean PM concentration under high RH conditions (light blue bars) in **a** the Beijing-Tianjin-Hebei region, **b** the Seoul metropolitan area, and **c** southern Japan. $PM_{2.5}$ concentrations are shown in (a), and PM_{10} concentrations are shown in (b, c) due to short-term data availability of $PM_{2.5}$ in the two regions (see text for details). The lines with markers indicate the ratio of mean $PM_{2.5}$ or PM_{10} concentrations under high RH conditions in spring to their annual means. The dashed lines are the linear regression lines of the ratios.

meteorological conditions. Here, the high RH conditions indicate days with a daily mean RH exceeding the 80th percentile of the seasonal mean. Note that observed PM_{10} concentrations are analyzed for South Korea and southern Japan in Fig. 1 because of the short-term $PM_{2.5}$ data availabilities in the regions (see details in Methods).

Regarding worsening trends in PM pollution, several previous studies have suggested that frequency of meteorological conditions conducive to severe PM pollution, such as stagnant weather, shallow atmospheric boundary layer, and weak winds, can increase due to climate change (or anthropogenic warming)^{10,12,13}. Most of previous studies, however, have focused on PM pollution in winter when anthropogenic emissions are high due to large heating/energy demands^{14,15}, and springtime PM pollution has received relatively less attention. Severe PM pollution has been frequently reported not only in winter but also in spring across Northeast Asia¹⁶. Along these lines, our study is motivated by the increasing trends in PM concentrations under high RH conditions in spring relative to the annual means (Fig. 1), and we aim to investigate if anthropogenic warming can be responsible for such increasing trends, which has not been previously answered.

Some studies have shown that the contributions of regional transport to PM pollution are large in spring as well as in winter in northern China¹⁷, South Korea¹⁸ and southern Japan¹⁹. Transboundary or long-range transported pollution frequently occurs over Northeast Asia during spring, and is often accompanied by cold fronts or migratory anticyclones²⁰. In addition, elevated RH during transboundary pollution is often observed in spring²¹,

which likely explains the large deviations in PM_{10} concentrations from their annual means under high RH conditions (Fig. 1b, c).

To examine the influence of anthropogenic warming on spring PM pollution with a special focus on transboundary pollution, we employ the pseudo-global-warming (PGW) strategy in which selected changes in a climate system (e.g., temperature changes) are added to or subtracted from historical climate simulations by modifying the initial and boundary conditions²². The PGW methods have been increasingly applied to many phenomena such as tropical cyclones^{23,24}, windstorms²⁵, runoff²⁶, and extreme snow events²⁷ in recent years, but to the authors' best knowledge few studies have applied the PGW approach to the influence of anthropogenic warming on spring PM pollution over Northeast Asia. To consider meteorological changes associated with anthropogenic warming from the past to the present, 50-year changes in meteorological variables (temperature, RH, wind, and geopotential height) estimated from reanalysis data are removed from the current meteorological fields similar to our previous study²⁸. The simulations that assume 50-year ago meteorology are referred to as PAST simulations, and the baseline simulations are referred to as PRESENT simulations (Methods). We examine a total of 24 pollution episodes in spring (see Methods) displaying high $PM_{2.5}$ concentrations and high RH conditions, using the Weather Research and Forecasting model coupled with chemistry (WRF-Chem model). The selected pollution episodes are categorized into three weather types (Supplementary Fig. 1), which is similar to the classifications reported in previous studies²⁹⁻³¹.

The PGW WRF-Chem simulations for 24 pollution episodes enable us to unravel the underlying mechanisms responsible for changes in spring PM pollution due to anthropogenic warming, including the influence of secondary aerosol formation. This contrasts with previous studies that used historical observational, reanalysis, and/or satellite data³²; examined only changes in meteorological conditions relevant to air quality³³; or analyzed global climate model simulations with no or simplified atmospheric chemistry processes^{10,34,35}.

Results

Changes in $PM_{2.5}$ due to meteorological changes

During the 50-year period, an increase in temperature is the most distinctive meteorological change reflecting global warming (Fig. 2a). Changes in low-level circulation are also observed, including anomalous southwesterly over inland southern China, East China Sea, and southern Japan, and anomalous northeasterly over the western North Pacific. The changes in winds at 850 hPa indicate enhanced westerly flows over South Korea (SKR) or southern Japan (SJP) (Supplementary Fig. 2). Based on the enhanced westerlies, the northern China or BTH region is defined as an upwind region and the SKR and SJP regions as downwind regions in this study. These changes in circulation delineate a previously reported²⁸ anomalous anticyclonic circulation centered around 25°N and 126°E. This circulation is induced by a greater temperature increase in northwestern Mongolia than in the western North Pacific²⁸. Because the overall air temperature increases during the 50-year period, RH decreases over most of the regions, except for the Yellow Sea, South Korea, East Sea, and part of southern Japan (Fig. 2b). The increases in RH in these regions are attributed to enhanced water vapor transport by the enhanced westerlies in these regions during the selected episodes (Supplementary Fig. 2).

The PRESENT simulations show that the concentrations of surface $PM_{2.5}$ (Fig. 2c) and individual $PM_{2.5}$ species (Fig. 2e, g, i) increase over the BTH, SKR, and SJP regions compared to the PAST simulations. Here, we present the maximum 2-day averaged $PM_{2.5}$ concentrations because the pollution episodes generally last for ~2 days, and it is noteworthy that the results with the maximum daily $PM_{2.5}$ concentrations are consistent with those presented here. The composite time series of $PM_{2.5}$ also show higher $PM_{2.5}$ concentrations in the three regions in the PRESENT simulations than in the PAST simulations (Fig. 2d, f, h), although the maximum $PM_{2.5}$ concentrations in the SKR region tend to be overestimated in the PRESENT simulations. The maximum increase and relative increase in median $PM_{2.5}$ are 14.9 $\mu\text{g m}^{-3}$ and 34.3% in the BTH, 17.0 $\mu\text{g m}^{-3}$ and 41.2% in the SKR,

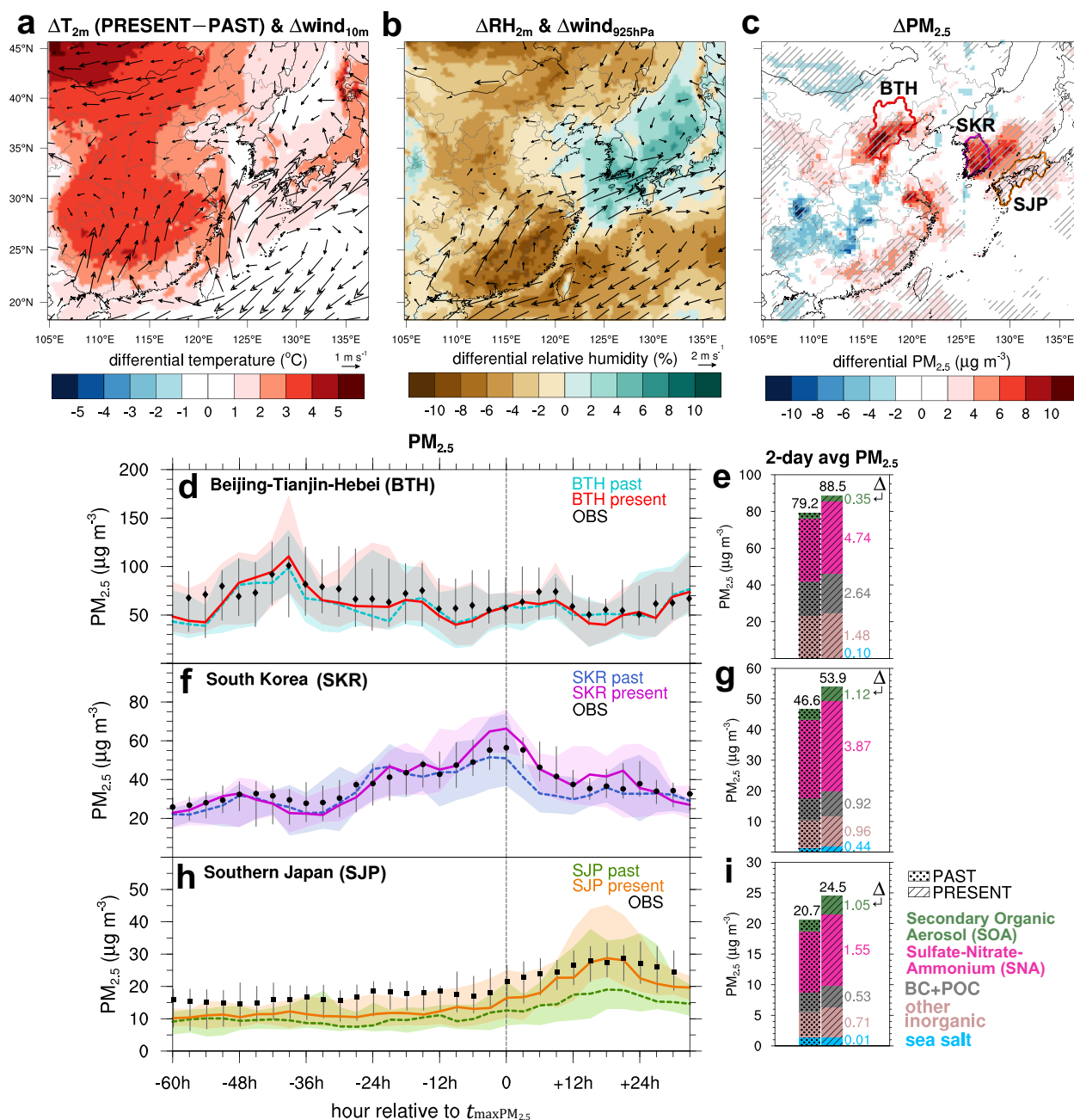


Fig. 2 | Differences in temperature, RH, and $PM_{2.5}$ concentration (PRESENT minus PAST). **a** Differences in temperature at 2 m and horizontal winds at 10 m, **b** relative humidity (RH) at 2 m and horizontal winds at 925 hPa, and **c** maximum 2-day average $PM_{2.5}$ near the surface between the PRESENT and PAST simulations (PRESENT minus PAST) averaged for the 24 episodes. Three regions are highlighted by thick lines in (c): Beijing-Tianjin-Hebei (BTH), South Korea (SKR), and southern Japan (SJP). The slanted lines in (c) indicate that the changes in $PM_{2.5}$ at least for 17 episodes (70% of the total 24 episodes) are in agreement (either positive or negative changes). **d, f, h** Composite time series of $PM_{2.5}$ averaged over the observation stations in the BTH, SKR, and SJP regions, respectively. The zero hour in the x-axis

represents the time of maximum $PM_{2.5}$ concentration in the SKR region ($t_{max PM_{2.5}}$). The solid (dashed) lines indicate the median $PM_{2.5}$ for the 24 episodes in the PRESENT (PAST) simulations; shadings indicate the interquartile ranges (25th and 75th percentiles); markers indicate the median values of observed $PM_{2.5}$; and the vertical lines show the interquartile ranges for the observations. **e, g, i** The maximum 2-day average $PM_{2.5}$ concentration and their composition in the PAST (dotted bar) and PRESENT (slanted bar) simulations in the BTH, SKR, and SJP regions, respectively. The numbers next to the bars indicate the differences in individual $PM_{2.5}$ species between the two simulations. The abbreviation “BC + POC” stands for the black carbon and primary organic carbon aerosol.

and $9.72 \mu g m^{-3}$ and 54.7% in the SJP regions, respectively. For the maximum 2-day averaged primary aerosols, black carbon (BC) and primary organic carbon (POC) aerosols, the increases in BC + POC concentrations in the PRESENT simulations relative to those in the PAST simulations are 14.1% in the BTH, 12.9% in the SKR, and 17.0% in the SKR regions (Fig. 2e, g, i). In both the PRESENT and PAST simulations, the median $PM_{2.5}$ for the

24 episodes shows that $PM_{2.5}$ concentrations are first elevated in the BTH region at around $t_{max PM_{2.5}} - 39$ h; a finding consistent with the results reported in previous studies^{36,37}. Here, $t_{max PM_{2.5}}$ indicates the time of maximum $PM_{2.5}$ concentration in the SKR region. The SKR region exhibits its maximum $PM_{2.5}$ concentration around 1.5 days later, and finally $PM_{2.5}$ in the SJP region reaches its peak about 15 h after $t_{max PM_{2.5}}$. These results

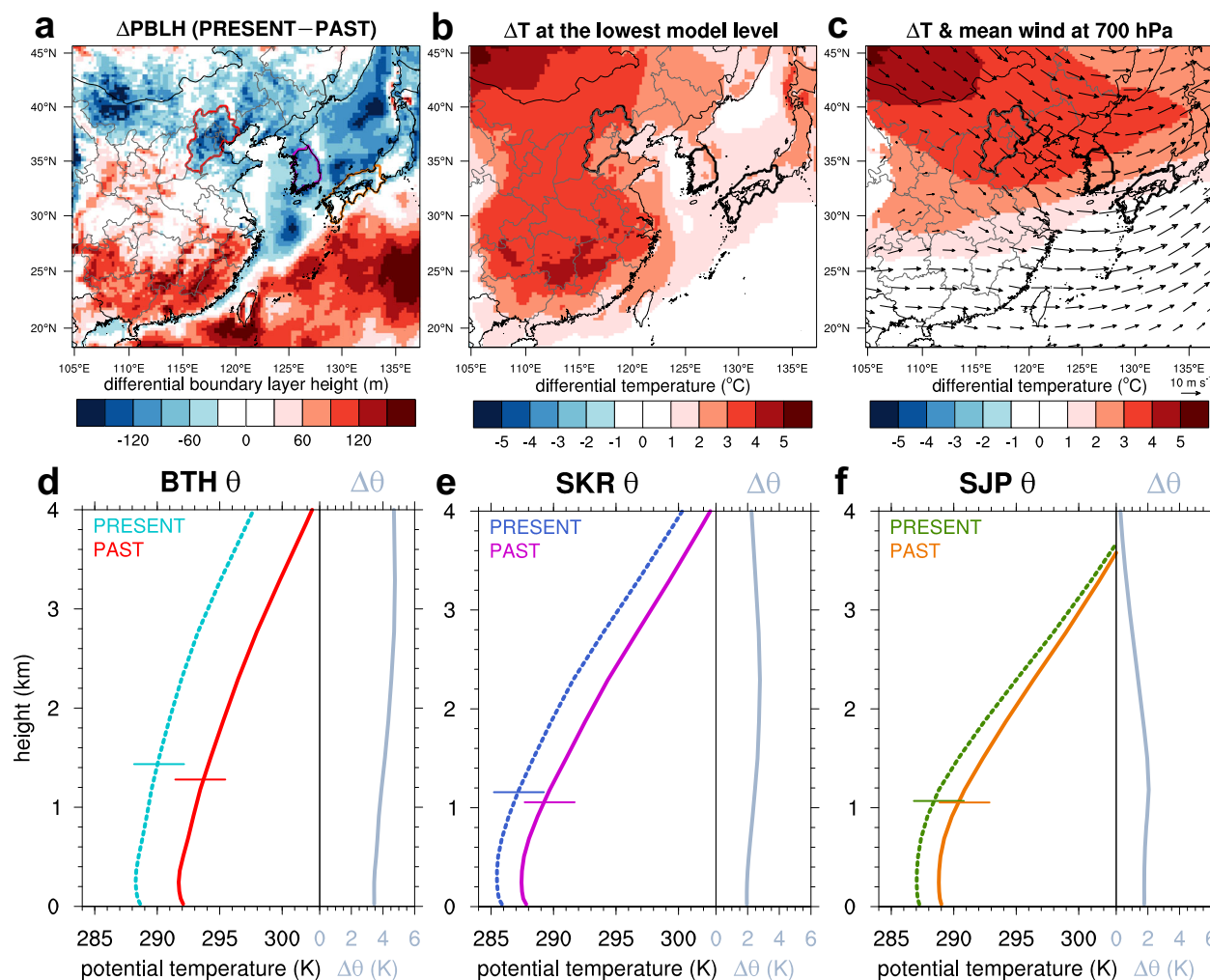


Fig. 3 | Differences in boundary layer height and lower- and upper-level temperature. **a** Differential boundary layer height, **b** temperature at the lowest model level, and **c** temperature at 700 hPa between the PRESENT and PAST simulations averaged for the 24 episodes. The vectors in (c) indicate the mean wind fields at 700 hPa averaged for the 24 episodes. **d–f** Vertical profiles of potential temperature (K) at 03 UTC averaged over all episodes in the PRESENT (solid line) and in the PAST

(dashed line) simulations in the Beijing-Tianjin-Hebei (BTH), South Korea (SKR), and Southern Japan (SJP), respectively. The gray lines attached to the vertical profiles of potential temperature indicate the vertical profiles of differential potential temperature (PRESENT minus PAST). The horizontal lines in (d–f) are the mean boundary layer heights for the 24 episodes in the two simulations.

indicate antecedent PM pollution in the BTH region and transboundary pollution in the downwind regions during the selected episodes. In other words, PM_{2.5} concentrations are first elevated in the BTH region and then pollutants are subsequently transported to the downwind regions.

Shallower boundary layer and higher PM_{2.5}

The increase in PM_{2.5} concentrations in the BTH region is attributed to the shallower boundary layer in the PRESENT simulation compared to the PAST simulation (Fig. 3a). The shallower boundary layer is most significant in the BTH region because of the advection of warm air in the upper levels from Eurasia (e.g., at the 700 hPa level, Fig. 3c), and the degree of warming is larger in the upper levels than near the surface (cf. Fig. 3b, c). Following the northwesterly (prevailing mean flow at 700 hPa for the selected episodes), the warmed air originating from high-latitude Eurasia is advected to East Asia during the selected episodes. This warmed air is potentially related to the accelerated snowmelt in spring due to anthropogenic warming^{38,39}. The differences in the vertical profiles of potential temperature between the two simulations indicate that the largest increase in potential temperature in the upper levels is observed in the BTH region (Fig. 3d), followed by the SKR region (Fig. 3e) and then the SJP region (Fig. 3f). The warmer air in the upper levels in the PRESENT simulations compared to the PAST simulations

inhibits the growth of the daytime boundary layer owing to increased stability. In the PRESENT simulations, the height of the daytime boundary layer at 03 UTC (around noon in local time) is lower by 155.4 m in the BTH, 101.7 m in the SKR, and 15.3 m in the SJP compared to the PAST simulations. In addition to our model simulations, the ERA5 boundary layer height under high RH conditions exhibits a decreasing trend in the BTH region in contrast to the weakly increasing trend in its spring mean values (Supplementary Fig. 3). Thus, human-induced warming is expected to degrade air quality in northern China where the shallow boundary layer due to warm air advection above the boundary layer is a primary driver of severe PM pollution in this region^{40–42}.

Budget analysis for BC + POC aerosols is performed, and the differences between the PAST (represented by dotted bars) and PRESENT (represented by slanted bars) simulations are analyzed (Fig. 4; also see Methods). The BC and POC aerosols can be regarded as tracers because they are chemically inert in the model. The budget analysis using primary aerosols provides an insight into the role of physical processes (not chemical processes) in PM_{2.5} changes between the two simulations. The PM_{2.5} concentration includes both primary and secondary aerosol concentrations, so it is hard to identify the role of physical processes such as mixing, transport, and deposition in changes in aerosol concentration when using PM_{2.5}

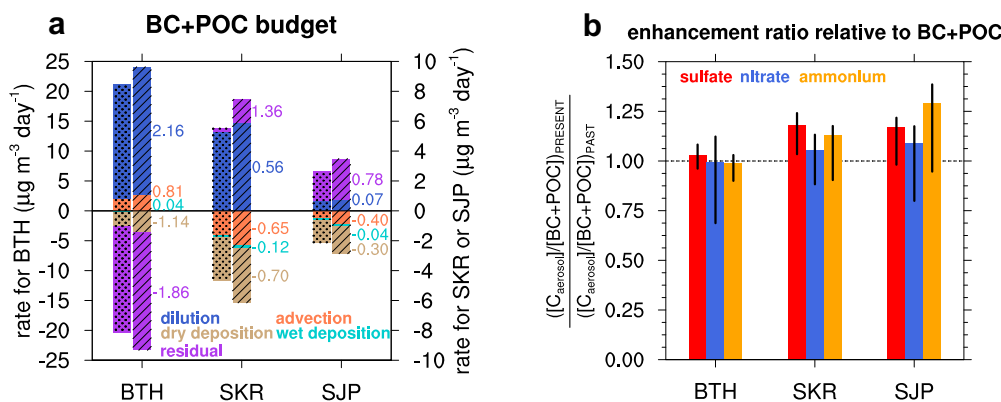


Fig. 4 | Contributions of physical processes to aerosols in the PRESENT and PAST simulations. Area-averaged budgets for a black and primary organic carbon aerosols (BC + POC). Note that the y-axis scale in the left (for BTH) is different from that in the right (for SKR or SJP). The numbers next to the right bars indicate the difference in each budget term between the two simulations (PRESENT minus PAST).

b Enhancement ratio of SNA aerosols relative to BC + POC aerosols in the PRESENT simulations to that in the PAST simulation. Here, C in the y-axis indicates the concentration of sulfate, nitrate, or ammonium aerosols. The vertical lines indicate the 25th and 75th percentiles of the 24 episodes.

concentration. The role of secondary aerosol formation by chemical processes is then identified by taking the ratio of secondary aerosol concentrations to primary aerosol concentrations in a later section.

In both the simulations, the dilution effect, defined as the emission rate divided by the boundary layer height, shows the largest positive contribution to the BC + POC budget in the BTH region. Most of the increases in the BC + POC concentrations in the heavily polluted BTH region are attributed to the difference in the dilution effect between the two simulations (indicated by the number in blue to the right of the bar in Fig. 4a). This finding confirms that the shallower boundary layer is the primary mechanism influencing the increase in BC + POC concentrations. In addition, it plays a major role in all three weather types (Supplementary Fig. 4).

Enhanced horizontal advection is the second contributing factor to the increase in BC + POC in the BTH region (Fig. 4a), particularly under type-2 and type-3 conditions (Supplementary Fig. 4e, f respectively). In Central-Eastern China, the prevailing southerly (type-2, Supplementary Fig. 1e), or southwesterly (type-3, Supplementary Fig. 1f) is reinforced by enhanced southwesterly anomalies due to the circulation change (Fig. 1a), resulting in an enhanced contribution of horizontal advection. The increase in the BC + POC concentration in the PRESENT simulation is compensated by the enhanced dry deposition and residual term in magnitude (Fig. 4a). In the PRESENT simulation, the increased contribution of dry deposition is attributed to the increased surface concentration of BC + POC. The residual term contributes negatively to both the simulations, indicating that aerosols are diffused upward from the surface layer to the upper layers in the BTH region^{43,44}.

Enhanced transboundary pollution

The residual terms in the SKR and SJP regions exhibit positive contributions to the BC + POC budgets, unlike in the BTH region, indicating that aerosols in the upper levels are transported and diffused downward in these regions. The positive contribution of vertical diffusion, that is, the residual term, implies that the aerosols are transported from upwind regions. Examples of the enhanced transboundary transport are shown in Supplementary Fig. 5 for the SKR region and in Supplementary Fig. 6 for the SJP region. In the PRESENT simulation, lots of aerosols are transported above boundary layer (boundary layer top is denoted by the thick-black line in Supplementary Fig. 5). At 21 UTC on 25 May 2016, the difference in BC + POC concentration near the surface over South Korea (beyond ~126.90°E, highlighted by the brown box) between the two simulations is very small and even shows negative values (Supplementary Fig. 5d). As the boundary layer grows in the daytime (00 UTC and 03 UTC), aerosols with high concentration in the free atmosphere are entrained and so aerosol concentration within the boundary layer increases in the PRESENT simulation. The increase in PM_{2.5}

concentration via vertical diffusion of elevated aerosol layers in the free atmosphere is consistent with previous findings⁴⁵. Supplementary Fig. 6 also illustrates a similar mechanism of the enhanced transboundary transport in the SJP region in the PRESENT simulation compared to the PAST simulation.

The increased contribution of vertical diffusion in the PRESENT simulation (positive values in purple in Fig. 4a) explains most of the increases in BC + POC, not only in the SKR but also in the farther downwind SJP region where local emissions are low. Enhanced aerosol transport to the SKR (Supplementary Fig. 2h) and SJP (Supplementary Fig. 2i) regions are supported by the strengthened westerlies at 850 hPa from the ERA5 trends on Day-1 and Day +1, respectively (see Methods for a detailed description of the pollution episode day). The stronger PM_{2.5} flux in the free atmosphere in the PRESENT simulations compared to the PAST simulations also confirms the enhanced upper-level transport (Supplementary Fig. 7a-c). Interestingly, the horizontal advection near the surface does not contribute to the increased BC + POC concentrations in the two downwind regions (negative values in orange in Fig. 4a). In addition, the boundary layer-integrated PM_{2.5} fluxes also exhibit small differences between the two simulations (Supplementary Fig. 7d-f). These results suggest that the enhanced upper-level transport of aerosols from the upwind regions contributes to the increase in PM_{2.5} concentrations in the SKR and SJP regions, indicating the enhanced transboundary pollution due to anthropogenic warming.

Enhanced secondary aerosol formation

To examine how much secondary aerosol formation can be enhanced relative to the changes in primary aerosols (e.g., BC + POC) in the PRESENT simulations, the sulfate, nitrate, and ammonium (SNA) aerosol concentrations are normalized by the BC + POC aerosol concentrations and the ratio in the PRESENT simulation is divided by the ratio in the PAST simulation. This ratio is called the enhancement ratio; for sulfate aerosol as an example, it is $\frac{([SO_4]/[BC+POC])_{PRESENT}}{([SO_4]/[BC+POC])_{PAST}}$. The assumption is that the impacts of physical processes (transport, mixing, and deposition, and others) on secondary aerosols can be ruled out by normalizing it to the concentrations of primary aerosols. An enhancement ratio larger than 1 indicates that secondary aerosols are chemically more produced in the PRESENT simulations than in the PAST simulations. Figure 4b compares the enhancement ratios averaged over 24 episodes in the three regions. The BTH region exhibits the enhancement ratios of ~1, meaning little change in chemical production of SNA aerosols between the PRESENT and PAST simulations. The mean enhancement ratios for sulfate, nitrate, and ammonium aerosols in the SKR region are 1.18, 1.06, and 1.13, respectively. A simple average of

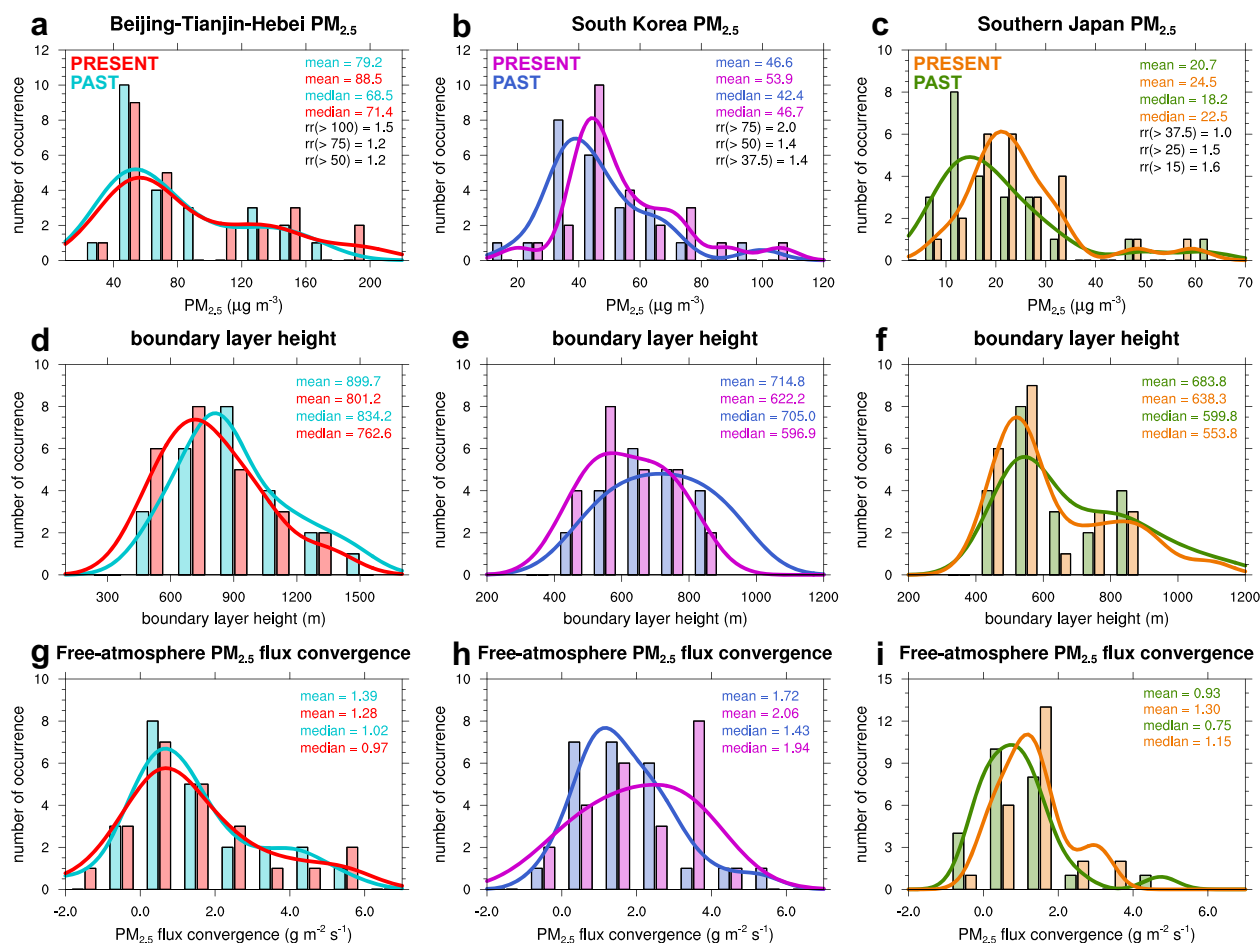


Fig. 5 | Comparison of PM_{2.5}, boundary layer height, and PM_{2.5} convergence between two simulations. Histogram of maximum 2-day average PM_{2.5} for the 24 episodes in the PRESENT and PAST simulations in the a Beijing-Tianjin-Hebei, b South Korea, and c southern Japan regions. The thick lines indicate the

probability density functions. The mean and median values are presented and rr indicates the risk ratio. d–f are the same as in (a–c), respectively but for boundary layer height. g–i are the same as in (a–c), respectively but for vertically-integrated PM_{2.5} flux convergence in the free atmosphere.

these ratios is 1.12, indicating that SNA aerosols are 12% more increased relative to primary aerosols due to anthropogenic warming in the SKR region. Similarly, in the SJP region, the simple average of the enhancement ratios for SNA aerosols is 1.18.

The changes in primary aerosol concentrations between the PRESENT and PAST simulations can be regarded as due to the enhanced atmospheric stability and/or the enhanced transboundary transport. Given that the primary aerosol concentrations are increased by ~14% in the BTH, ~13% in the SKR, and ~17% in the SJP regions in the PRESENT simulations relative to those in the PAST simulations (Fig. 2e, g, i), the secondary aerosol formation is enhanced by a factor of 1.12 in the SKR region and of 1.18 in the SJP region on average compared to the change in primary aerosol concentrations. The larger secondary aerosol formation in the SKR and SJP regions than in the BTH region can be attributed the larger increases in RH in the SKR and SJP regions (Fig. 2b and Supplementary Fig. 8), which promotes the formation of secondary inorganic aerosols^{46–48}. So, it can be concluded that the enhanced moisture transport (Supplementary Fig. 2g–i) and elevated RH contribute to an increase in the secondary aerosols during transboundary pollution events.

Discussion

The present study highlights that anthropogenic warming can worsen springtime PM pollution across Northeast Asia, not only in the upwind region (BTH region) but also in the downwind regions (SKR and SJP regions). Histograms of PM_{2.5} concentrations in the three regions show increased frequencies of high PM pollution levels as well as increased mean

and median values (Fig. 5a–c). For example, in the BTH region, the risk ratio of severe PM_{2.5} pollution with a maximum 2-day average PM_{2.5} > 100 μg m⁻³ is 1.5 times higher in the PRESENT simulation than in the PAST simulation. Similarly, the risk ratio of PM_{2.5} > 75 μg m⁻³ in the SKR region is doubled. The mechanisms responsible for the worsening PM pollution differ between the upwind (BTH) and downwind regions (SKR and SJP). In the heavily polluted northern China, the primary mechanism is a reduction in the boundary layer height due to the warmed-air advection in the upper levels from high-latitude Eurasia, thereby increasing atmospheric stability. The histogram of the boundary layer height exhibits a significant leftward shift, with a decrease in the mean value of 98.5 m in the BTH region (Fig. 5d). In the downwind regions, enhanced long-range transport of pollutants and entrainment of aloft-polluted air masses increase PM_{2.5} concentrations near the surface. The enhanced transboundary pollution in the downwind regions, particularly in the far-downwind region (SJP), is supported by the rightward shifts of the histograms for PM_{2.5} flux convergence in the free atmosphere (Fig. 5h, i). However, such an increase is not observed in the upwind region (Fig. 5g). Considerable increases in RH are also found in the downwind regions owing to enhanced water vapor transport during transboundary pollution episodes. Consequently, the formation of secondary inorganic aerosols is enhanced, exacerbating PM pollution in downwind regions.

This study identifies the distinct physical and chemical processes responsible for the elevated PM levels in the upwind and downwind regions during springtime transboundary pollution events, thus providing insights into the influence of global warming on air quality over Northeast Asia. The

results suggest that despite reduced emissions, poorer air quality that deviates from the overall conditions can occur under more conducive meteorological conditions owing to global warming. Therefore, our findings underscore the need for effective and proactive international cooperation to reduce the air pollution exacerbated by anthropogenic warming. In this study, we focus on the influence of anthropogenic warming on air quality using PGW simulations. There can be other mechanisms or processes that worsen PM pollution, such as aerosol-cloud interactions and aerosol-boundary layer interactions. Further studies are required to elucidate other relevant mechanisms and the potential interplay between them.

Methods

Reanalysis data and trend computation for WRF-Chem simulations

The ERA5 reanalysis data⁴⁹ have been used to compute changes in the meteorological variables over the last 50 years and to drive WRF-Chem simulations. We calculate the linear trends of various meteorological variables for high RH days (Supplementary Fig. 2) using the 42-year ERA5 reanalysis data (1979–2020) at a resolution of $0.25^\circ \times 0.25^\circ$. The variables considered are temperature, sea surface temperature, RH, horizontal wind, and geopotential height. The linear trends in meteorological variables calculated using the ERA5 data are assumed to be largely attributable to anthropogenic warming, considering that the recent observed trend can be reproduced by climate models only when including greenhouse gas increases^{50,51}. High RH days were selected when the daily mean RH is $>65\%$ and the daily precipitation is $<1 \text{ mm day}^{-1}$ over the Seoul metropolitan area, SMA ($36.75^\circ\text{--}38.5^\circ\text{N}$, $125.25^\circ\text{--}128^\circ\text{E}$). The average values of the individual variables on the selected high RH days (referred to as Day + 0) for each year (42 data points) are used to compute their linear trends at each model level and grid. Linear trends are then used to compute the 50-year changes in the individual variables. In the PAST simulations, the sensitivity simulations and individual meteorological variables at each grid are altered as follows.

$$V_{\text{PAST}} = V_{\text{PRESENT}} - V_{\Delta} \quad (1)$$

Where, V indicates the meteorological variables (e.g., temperature, RH, and winds) in the PAST and PRESENT climates (denoted as subscripts) and V_{Δ} is the change in each variable during the 50-year period. Linear trends for the days prior to or after Day + 0 are also computed separately. For example, all fields three days prior to Day + 0 are averaged for each year, and their trends are referred to as the trends of Day–3. The ERA5 trends of temperature, RH, water vapor mixing ratio, and horizontal winds at 850 hPa on Day–3, Day–1, and Day + 1 are shown as examples in Supplementary Fig. 2. In the PAST simulations, the computed changes in individual meteorological variables (i.e., V_{Δ}) on Day–3 through Day + 3 are subtracted from the current meteorological variables on the corresponding days.

Surface observation data

The $\text{PM}_{2.5}$ observation data in South Korea since 2015 are obtained from Air Korea (<https://www.airkorea.or.kr/>). We select inland stations (total: 111) having at least 70% data availability since 2015 for model evaluation. The station-wide averaged $\text{PM}_{2.5}$ is presented in Fig. 2f. Note that episodes since 2015 are shown in Fig. 2f for South Korea because $\text{PM}_{2.5}$ observations have been available only since 2015. For the long-term trend of PM_{10} since 2001 (Fig. 1), we use PM_{10} because it is only available for a long-term period. In Fig. 1, the days influenced by Yellow Dust are excluded. Supplementary Fig. 9 shows the ratio of mean $\text{PM}_{2.5}$ concentrations under high RH conditions to the annual mean since 2015 when $\text{PM}_{2.5}$ data are available. The correlation coefficient between the ratios using $\text{PM}_{2.5}$ and PM_{10} over the Seoul metropolitan area is 0.95.

Full-year $\text{PM}_{2.5}$ data for the BTH region (77 stations) since 2015 are acquired from <https://quotsoft.net/air/> (originally operated by the China National Environmental Monitoring Centre). We utilized $\text{PM}_{2.5}$ observation data in Beijing (39.95°N , 116.47°E) measured and operated by the U.S. Embassy (<http://www.stateair.net/web/historical/1/1.html>) for the years

2013 and 2014. We compared the hourly $\text{PM}_{2.5}$ data at the U.S. Embassy Beijing station with the station-wide averaged $\text{PM}_{2.5}$ data in the BTH region from environmental monitoring stations in China (77 stations) to estimate hourly $\text{PM}_{2.5}$ concentrations in the BTH region for 2013 and 2014. Linear regression for the year 2016 shows a relatively high correlation coefficient (0.821) between the $\text{PM}_{2.5}$ at the Beijing station and the station-wide averaged $\text{PM}_{2.5}$ in the BTH region. The slope and intercept values of the linear regression are used to estimate the BTH-averaged $\text{PM}_{2.5}$, for 2013 and 2014. For the long-term trend shown in Fig. 1, we use daily $\text{PM}_{2.5}$, that are estimated by a machine learning model⁵², which are originally available at 6-h intervals (<https://doi.org/10.5281/zenodo.6372847>).

The Japanese $\text{PM}_{2.5}$ data are obtained from the National Institute for Environmental Studies (<https://www.nies.go.jp>), and the data for 252 stations located in southern Japan are used for the model evaluation. For the long-term trends, PM_{10} data are also used for Japan because of the short-term availability of $\text{PM}_{2.5}$ over Japan. Days influenced by Yellow Dust are also excluded for the computation of PM_{10} averages. The ratio of mean $\text{PM}_{2.5}$ under high RH conditions to the annual mean is also shown in Supplementary Fig. 9c since 2011 when $\text{PM}_{2.5}$ data are available. The correlation coefficient between the ratios using $\text{PM}_{2.5}$ and PM_{10} over the southern Japan is 0.97.

WRF-Chem simulations

We use the recently updated WRF-Chem model⁵³, and the model configuration is identical to that used in a previous study²⁸, except for the initial and boundary meteorological conditions for the PAST simulations. The essential model configuration is described below in brief: meteorological initial and boundary conditions are provided from the ERA5 reanalysis data at 3 h intervals, chemical boundary conditions are provided from the CAMS reanalysis⁵⁴, anthropogenic emissions used are REASv3.2⁵⁵, biogenic emissions are computed by the MEGAN v2.04⁵⁶ implemented in the WRF-Chem model, biomass burning emissions used are GFASv1.2^{57,58}, the gas-aerosol chemistry mechanism is MOZART-MOSAIC^{59,60}, and the horizontal resolution is 20 km. Altered variables in the PAST simulations are used as the initial and boundary conditions for the meteorology, and four-dimensional data assimilation analysis nudging is used above the boundary layer. Most of the simulations start four days prior to Day + 0 and end two or three days after Day3 + 0.

To select pollution episodes in spring (March–May), we use long-term WRF-Chem simulations from 2013 to 2019. Pollution episodes refer to days with high RH and high $\text{PM}_{2.5}$ concentrations obtained either in the simulations or surface observations. These episodes are classified into three weather types. Type-1 is influenced by a high-pressure system that is initially centers in northern China and then slowly moves eastward to the Korean Peninsula. Under the influence of this lingering high-pressure system, type-1 is characterized by high $\text{PM}_{2.5}$ concentrations over both the BTH and SMA regions (Supplementary Fig. 1a, d). The criteria for type-1 episodes are provided as follows: (1) Either simulated or observed daily $\text{PM}_{2.5}$ averaged over the SMA for a 3-day period (including two days prior to Day + 0) is greater than its seasonal mean + $0.75 \times$ standard deviation, (2) Daily RH over the SMA or aerosol water content is greater than 54.9% or $10 \mu\text{g m}^{-3}$, respectively at least once during the 3-day period, (3) Wind speed at 925 hPa is smaller than 7 m s^{-1} , (4) Either simulated or observed daily $\text{PM}_{2.5}$ averaged over the BTH is greater than its seasonal mean plus $0.75 \times$ standard deviation for at least once during the 3-day period, and (5) Daily RH over the BTH is greater than 50% at least once during the 3-day period. Type-2 episodes are influenced by an extended western North Pacific subtropical high (Supplementary Fig. 1b), causing southwesterly that bring in moist and polluted air from southern and eastern China. This results in high RH and $\text{PM}_{2.5}$ concentrations over South Korea. The criteria for type-2 episodes are as follows: (1) Either simulated or observed daily $\text{PM}_{2.5}$ averaged over the SMA for the 3-day period (including the two days prior to Day + 0) is greater than a threshold (= seasonal mean + $0.75 \times$ standard deviation), (2) Daily RH over the SMA or aerosol water content is greater than 54.9% or $10 \mu\text{g m}^{-3}$, respectively at least once during the 3-day period, (3) Wind speed

at 925 hPa is greater than 7.5 m s^{-1} , (4) Daily RH over east China (29° – 35°N , 115° – 122°E) is greater than 60%, and (5) Daily $\text{PM}_{2.5}$ over east China is greater than its seasonal mean. Both type-1 and type-2 episodes typically last for several days. In comparison, type-3 episodes are characterized by strong westerly lasting for short durations (~ 1 – 2 d). The criteria for type-3 episodes are as follows: (1) Daily $\text{PM}_{2.5}$ over the SMA on Day + 0 is greater than the seasonal mean + $0.75 \times$ standard deviation, (2) Daily RH over the SMA or aerosol water content is greater than 54.9% or greater than $10 \mu\text{g m}^{-3}$, respectively on Day + 0, and (3) Wind speed at 925 hPa is greater than 7.5 m s^{-1} . The weather patterns of the three episodes in our study are qualitatively similar to those classified as synoptic weather patterns 1, 2, and 4 in a previous study²⁹. Selected cases are presented in Supplementary Table 1.

Budget analysis

Aerosol budget analyses are conducted for primary carbon (BC + POC) aerosols in the lowest model layer. It is to be noted that other inorganic (OIN) aerosol budgets are not analyzed because both anthropogenic and natural (dust) sources contribute to OIN aerosols in the WRF-Chem model. The directly computed budget terms include the aerosol concentration (and so the tendency), dilution, dry deposition, wet deposition, and horizontal advection. The dilution term is calculated by dividing the emission rate by the boundary layer height, because the budget analysis focuses on the lowest model layer. Therefore, it represents the contribution of emissions to the aerosol concentration near the surface, under the assumption that the emitted aerosols are well mixed within the boundary layer. The contributions of vertical diffusion from/to the boundary layer to/from the free atmosphere is not directly output. No chemical transformation of the primary carbon aerosols is considered in the model; thus, the residual term can be interpreted as the contribution of vertical diffusion. Vertical diffusion has two effects: venting and entrainment. Venting is a negative contribution that refers to the venting of pollutants from the boundary layer into the free atmosphere, whereas entrainment is a positive contribution that refers to the capture of pollutants in the free atmosphere into the boundary layer. Entrainment is associated with the horizontal transport of pollutants in the free atmosphere and the mixing of pollutants when the boundary layer grows during daytime.

Data availability

The ERA5 reanalysis data can be obtained from <https://cds.climate.copernicus.eu/cdsapp#!/home>. The $\text{PM}_{2.5}$ and PM_{10} observation data in South Korea can be obtained from Air Korea (<https://www.airkorea.or.kr/>). Full-year hourly $\text{PM}_{2.5}$ data for the BTH region since 2015 are available from <https://quotsoft.net/air/>. The U.S. Embassy $\text{PM}_{2.5}$ data are available from <http://www.stateair.net/web/historical/1/1.html>. The long-term 6-hourly $\text{PM}_{2.5}$ data can be downloaded from <https://doi.org/10.5281/zenodo.6372847>. Japanese $\text{PM}_{2.5}$ are available from the National Institute for Environmental Studies (<https://www.nies.go.jp>). The datasets used and/or analyzed during the current study available from the corresponding author on reasonable request.

Code availability

The updated WRF-Chem codes are available at <https://doi.org/10.5281/zenodo.5895233>.

Received: 26 October 2023; Accepted: 19 February 2024;

Published online: 28 February 2024

References

- Zhang, M., Song, Y. & Cai, X. A health-based assessment of particulate air pollution in urban areas of Beijing in 2000–2004. *Sci. Total Environ.* **376**, 100–108 (2007).
- Turner, M. C. et al. Outdoor air pollution and cancer: an overview of the current evidence and public health recommendations. *CA Cancer J. Clin.* **70**, 460–479 (2020).
- Son, J.-Y., Lee, J.-T., Kim, K.-H., Jung, K. & Bell, M. L. Characterization of fine particulate matter and associations between particulate chemical constituents and mortality in Seoul, Korea. *Environ. Health Perspect.* **120**, 872–878 (2012).
- Zou, J. et al. Aerosol chemical compositions in the North China Plain and the impact on the visibility in Beijing and Tianjin. *Atmos. Res.* **201**, 235–246 (2018).
- Liu, J. et al. Increased aerosol extinction efficiency hinders visibility improvement in Eastern China. *Geophys. Res. Lett.* **47**, e2020GL090167 (2020).
- Yang, X., Zhao, C., Guo, J. & Wang, Y. Intensification of aerosol pollution associated with its feedback with surface solar radiation and winds in Beijing. *J. Geophys. Res. -Atmos.* **121**, 4093–4099 (2016).
- Hu, B. et al. Quantification of the impact of aerosol on broadband solar radiation in North China. *Sci. Rep.* **7**, 44851 (2017).
- Duan, L. et al. Acid deposition in Asia: emissions, deposition, and ecosystem effects. *Atmos. Environ.* **146**, 55–69 (2016).
- Mahowald, N. M. et al. Aerosol deposition impacts on land and ocean carbon cycles. *Curr. Clim. Change Rep.* **3**, 16–31 (2017).
- Chen, H., Wang, H., Sun, J., Xu, Y. & Yin, Z. Anthropogenic fine particulate matter pollution will be exacerbated in eastern China due to 21st century GHG warming. *Atmos. Chem. Phys.* **19**, 233–243 (2019).
- Ryu, Y.-H., Min, S.-K. & Hodzic, A. Recent decreasing trends in surface $\text{PM}_{2.5}$ over East Asia in the winter-spring season: different responses to emissions and meteorology between upwind and downwind regions. *Aerosol Air Qual. Res.* **21**, 200654 (2021).
- Cai, W., Li, K., Liao, H., Wang, H. & Wu, L. Weather conditions conducive to Beijing severe haze more frequent under climate change. *Nat. Clim. Change* **7**, 257–262 (2017).
- Han, Z., Zhou, B., Xu, Y., Wu, J. & Shi, Y. Projected changes in haze pollution potential in China: an ensemble of regional climate model simulations. *Atmos. Chem. Phys.* **17**, 10109–10123 (2017).
- Zhao, S. et al. Impact of climate change on Siberian high and wintertime air pollution in China in past two decades. *Earths Future* **6**, 118–133 (2018).
- Li, J. et al. Winter particulate pollution severity in North China driven by atmospheric teleconnections. *Nat. Geosci.* **15**, 349–355 (2022).
- Chen, S. et al. Inter-annual variation of the spring haze pollution over the North China Plain: Roles of atmospheric circulation and sea surface temperature. *Int. J. Climatol.* **39**, 783–798 (2019).
- Chen, D. et al. Impact of inter-annual meteorological variation from 2001 to 2015 on the contribution of regional transport to $\text{PM}_{2.5}$ in Beijing, China. *Atmos. Environ.* **260**, 118545 (2021).
- Kumar, N. et al. Contributions of international sources to $\text{PM}_{2.5}$ in South Korea. *Atmos. Environ.* **261**, 118542 (2021).
- Ikeda, K. et al. Source region attribution of $\text{PM}_{2.5}$ mass concentrations over Japan. *Geochem. J.* **49**, 185–194 (2015).
- Marumoto, K., Hayashi, M. & Takami, A. Atmospheric mercury concentrations at two sites in the Kyushu Islands, Japan, and evidence of long-range transport from East Asia. *Atmos. Environ.* **117**, 147–155 (2015).
- Eck, T. F. et al. Influence of cloud, fog, and high relative humidity during pollution transport events in South Korea: aerosol properties and $\text{PM}_{2.5}$ variability. *Atmos. Environ.* **232**, 117530 (2020).
- Brogli, R., Heim, C., Mensch, J., Sørland, S. L. & Schär, C. The pseudo-global-warming (PGW) approach: methodology, software package PGW4ERA5 v1.1, validation, and sensitivity analyses. *Geosci. Model Dev.* **16**, 907–926 (2023).
- Ito, R., Takemi, T. & Arakawa, O. A possible reduction in the severity of typhoon wind in the Northern part of Japan under global warming: a case study. *Sola* **12**, 100–105 (2016).
- Gutmann, E. D. et al. Changes in Hurricanes from a 13-yr convection-permitting pseudo-global warming simulation. *J. Clim.* **31**, 3643–3657 (2018).

25. Sethunadh, J., Letson, F. W., Barthelmie, R. J. & Pryor, S. C. Assessing the impact of global warming on windstorms in the northeastern United States using the pseudo-global-warming method. *Nat. Hazards* **117**, 2807–2834 (2023).
26. Rasmussen, R. et al. High-resolution coupled climate runoff simulations of seasonal snowfall over Colorado: a process study of current and warmer climate. *J. Clim.* **24**, 3015–3048 (2011).
27. Chen, G., Wang, W.-C., Cheng, C.-T. & Hsu, H.-H. Extreme snow events along the coast of the Northeast United States: potential changes due to global warming. *J. Clim.* **34**, 2337–2353 (2021).
28. Ryu, Y.-H. & Min, S.-K. Greenhouse warming and anthropogenic aerosols synergistically reduce springtime rainfall in low-latitude East Asia. *npj Clim. Atmos. Sci.* **5**, 1–10 (2022).
29. Zhang, Y. et al. Impact of synoptic weather patterns and inter-decadal climate variability on air quality in the North China Plain during 1980–2013. *Atmos. Environ.* **124**, 119–128 (2016).
30. Jeon, W. et al. Impact of varying wind patterns on PM10 concentrations in the Seoul Metropolitan Area in South Korea from 2012 to 2016. *J. Appl. Meteorol. Clim.* **58**, 2743–2754 (2019).
31. Lee, D. et al. Relationship between synoptic weather pattern and surface particulate matter (PM) concentration during winter and spring seasons over South Korea. *J. Geophys. Res. Atmos.* **127**, e2022JD037517 (2022).
32. Zhang, X., Zhong, J., Wang, J., Wang, Y. & Liu, Y. The interdecadal worsening of weather conditions affecting aerosol pollution in the Beijing area in relation to climate warming. *Atmos. Chem. Phys.* **18**, 5991–5999 (2018).
33. Xu, Y. et al. Influence of human activities on wintertime haze-related meteorological conditions over the Jing–Jin–Ji region. *Engineering* **7**, 1185–1192 (2021).
34. Qiu, L., Yue, X., Hua, W. & Lei, Y.-D. Projection of weather potential for winter haze episodes in Beijing by 1.5 °C and 2.0 °C global warming. *Adv. Clim. Change Res.* **11**, 218–226 (2020).
35. Li, K., Liao, H., Cai, W. & Yang, Y. Attribution of anthropogenic influence on atmospheric patterns conducive to recent most severe haze over Eastern China. *Geophys. Res. Lett.* **45**, 2072–2081 (2018).
36. Lee, S., Ho, C.-H. & Choi, Y.-S. High-PM10 concentration episodes in Seoul, Korea: background sources and related meteorological conditions. *Atmos. Environ.* **45**, 7240–7247 (2011).
37. Kim, H., Zhang, Q. & Sun, Y. Measurement report: characterization of severe spring haze episodes and influences of long-range transport in the Seoul metropolitan area in March 2019. *Atmos. Chem. Phys.* **20**, 11527–11550 (2020).
38. Diffenbaugh, N. S., Scherer, M. & Ashfaq, M. Response of snow-dependent hydrologic extremes to continued global warming. *Nat. Clim. Change* **3**, 379–384 (2013).
39. Paik, S. & Min, S.-K. Quantifying the anthropogenic greenhouse gas contribution to the observed spring snow-cover decline using the CMIP6 multimodel ensemble. *J. Clim.* **33**, 9261–9269 (2020).
40. Yan, Y. et al. Long-term planetary boundary layer features and associated PM2.5 pollution anomalies in Beijing during the past 40 years. *Theor. Appl. Climatol.* **151**, 1787–1804 (2023).
41. Su, T., Li, Z. & Kahn, R. Relationships between the planetary boundary layer height and surface pollutants derived from lidar observations over China: regional pattern and influencing factors. *Atmos. Chem. Phys.* **18**, 15921–15935 (2018).
42. Li, Q., Zhang, H., Cai, X., Song, Y. & Zhu, T. The impacts of the atmospheric boundary layer on regional haze in North China. *npj Clim. Atmos. Sci.* **4**, 1–10 (2021).
43. Fan, Q. et al. Process analysis of regional aerosol pollution during spring in the Pearl River Delta region, China. *Atmos. Environ.* **122**, 829–838 (2015).
44. Chen, T.-F., Chang, K.-H. & Lee, C.-H. Simulation and analysis of causes of a haze episode by combining CMAQ-IPR and brute force source sensitivity method. *Atmos. Environ.* **218**, 117006 (2019).
45. Lee, H.-J., Jo, H.-Y., Kim, S.-W., Park, M.-S. & Kim, C.-H. Impacts of atmospheric vertical structures on transboundary aerosol transport from China to South Korea. *Sci. Rep.* **9**, 13040 (2019).
46. Zheng, B. et al. Heterogeneous chemistry: a mechanism missing in current models to explain secondary inorganic aerosol formation during the January 2013 haze episode in North China. *Atmos. Chem. Phys.* **15**, 2031–2049 (2015).
47. Zheng, G. J. et al. Exploring the severe winter haze in Beijing: the impact of synoptic weather, regional transport and heterogeneous reactions. *Atmos. Chem. Phys.* **15**, 2969–2983 (2015).
48. Shao, J. et al. Heterogeneous sulfate aerosol formation mechanisms during wintertime Chinese haze events: air quality model assessment using observations of sulfate oxygen isotopes in Beijing. *Atmos. Chem. Phys.* **19**, 6107–6123 (2019).
49. Hersbach, H. et al. The ERA5 global reanalysis. *Q. J. Roy. Meteor. Soc.* **146**, 1999–2049 (2020).
50. Seong, M.-G., Min, S.-K., Kim, Y.-H., Zhang, X. & Sun, Y. Anthropogenic greenhouse gas and aerosol contributions to extreme temperature changes during 1951–2015. *J. Clim.* **34**, 857–870 (2021).
51. Sun, Y. et al. Understanding human influence on climate change in China. *Natl. Sci. Rev.* **9**, nwab113 (2022).
52. Zhong, J. et al. Reconstructing 6-hourly PM_{2.5} datasets from 1960 to 2020 in China. *Earth Syst. Sci. Data* **14**, 3197–3211 (2022).
53. Ryu, Y.-H. & Min, S.-K. Improving wet and dry deposition of aerosols in WRF-Chem: Updates to below-cloud scavenging and coarse-particle dry deposition. *J. Adv. Model. Earth Syst.* **14**, e2021MS002792 (2022).
54. Inness, A. et al. The CAMS reanalysis of atmospheric composition. *Atmos. Chem. Phys.* **19**, 3515–3556 (2019).
55. Kurokawa, J. & Ohara, T. Long-term historical trends in air pollutant emissions in Asia: Regional Emission inventory in ASia (REAS) version 3. *Atmos. Chem. Phys.* **20**, 12761–12793 (2020).
56. Guenther, A. et al. Estimates of global terrestrial isoprene emissions using MEGAN (Model of Emissions of Gases and Aerosols from Nature). *Atmos. Chem. Phys.* **6**, 3181–3210 (2006).
57. Kaiser, J. W. et al. Biomass burning emissions estimated with a global fire assimilation system based on observed fire radiative power. *Biogeosciences* **9**, 527–554 (2012).
58. Rémy, S. et al. Description and evaluation of the tropospheric aerosol scheme in the European Centre for Medium-Range Weather Forecasts (ECMWF) Integrated Forecasting System (IFS-AER, cycle 45R1). *Geosci. Model Dev.* **12**, 4627–4659 (2019).
59. Knote, C. et al. Simulation of semi-explicit mechanisms of SOA formation from glyoxal in aerosol in a 3-D model. *Atmos. Chem. Phys.* **14**, 6213–6239 (2014).
60. Knote, C., Hodzic, A. & Jimenez, J. L. The effect of dry and wet deposition of condensable vapors on secondary organic aerosols concentrations over the continental US. *Atmos. Chem. Phys.* **15**, 1–18 (2015).

Acknowledgements

We thank Anqi Liu for helping with the acquisition of Chinese observational data. Y.-H.R. was funded by a National Research Foundation of Korea (NRF) grant funded by the Korean Government (MSIT) (RS-2023-00274625) and by the Yonsei University Research Fund of 2023 (2023-22-0130). Y.-H.R. also acknowledges the support from KISTI (KSC-2023-CRE-0040). S.-K.M. was funded by a National Research Foundation of Korea grant from the Korean Government (NRF2021R1A2C300736) and the Human Resource Program for Sustainable Environment in the 4th Industrial Revolution Society.

Author contributions

Y-HR and S-KM conceived this study. Y-HR performed numerical simulations, analyzed the results, and wrote the original draft. S-KM suggested the design and methods of numerical experiments and discussed results. All authors read and approved the final manuscript.

Competing interests

The authors declare no competing interests.

Additional information

Supplementary information The online version contains supplementary material available at

<https://doi.org/10.1038/s41612-024-00603-7>.

Correspondence and requests for materials should be addressed to Seung-Ki Min.

Reprints and permissions information is available at <http://www.nature.com/reprints>

Publisher's note Springer Nature remains neutral with regard to jurisdictional claims in published maps and institutional affiliations.

Open Access This article is licensed under a Creative Commons Attribution 4.0 International License, which permits use, sharing, adaptation, distribution and reproduction in any medium or format, as long as you give appropriate credit to the original author(s) and the source, provide a link to the Creative Commons licence, and indicate if changes were made. The images or other third party material in this article are included in the article's Creative Commons licence, unless indicated otherwise in a credit line to the material. If material is not included in the article's Creative Commons licence and your intended use is not permitted by statutory regulation or exceeds the permitted use, you will need to obtain permission directly from the copyright holder. To view a copy of this licence, visit <http://creativecommons.org/licenses/by/4.0/>.

© The Author(s) 2024